RSC Advances

ROYAL SOCIETY OF CHEMISTRY

www.rsc.org/advances

Facile preparation of reduced graphene oxide supported PtNi alloyed nanosnowflakes with highly catalytic activity

Pei Song, Jiu-Ju Feng, Shu-Xian Zhong, Su-Su Huang, Jian-Rong Chen, Ai-Jun Wang*

College of Chemistry and Life Science, College of Geography and Environmental Science, Zhejiang Normal University, Jinhua, 321004, China

**Corresponding author: ajwang@zjnu.cn (AJW), Tel./Fax: +86 579 82282269.*

Abstract

A facile hydrothermal strategy was designed for the preparation of alloyed PtNi nanosnowflakes supported on reduced graphene oxide (PtNi nanosnowflakes/RGO), with the assistance of N, N-dimethylformamide (DMF) as the solvent and reductant, and ethylenediamine as the surfactant and capping agent. The as-obtained nanocomposites were mainly characterized by transmission electron microscopy (TEM), X-ray diffraction (XRD), X-ray photoelectron spectroscopy (XPS) and Raman spectroscopy, which showed enhanced catalytic activity and better stability over commercial Pt/C (10 wt. %) in the catalytic reduction of *p*-nitrophenol to *p*-aminophenol.

Keywords: Reduced graphene oxide; Bimetallic PtNi nanosnowflake; Catalyst; *p*-Nitrophenol

1. Introduction

p-Aminophenol (*p*-AP) is an vital intermediate for the synthesis of analgesic and antipyretic drugs,[1, 2] which can be further explored as photographic developer, corrosion inhibitor, anticorrosion-lubricant, and hair-dyeing agent.[3, 4] Conventionally, *p*-AP is produced by multi-step iron-acid reduction of *p*-nitrochlorobenzene (*p*-NB) or *p*-nitrophenol (*p*-NP), which causes severe environmental problems by generating a large amount of Fe-FeO sludge.[5, 6] To meet the growing demand of *p*-AP, it is important to develop an efficient and green approach for the directly catalytic hydrogenation of *p*-NP.[7-9] Moreover, the reduction process of *p*-NP may be extended for the treatment of *p*-NP wastewater. *p*-NP is extensively used in a wide range of industries, such as pharmaceutical, leather, printing, paint and textile, which leaves a large amount of wastewater with a high content of residual pollutants. The aromatic contaminants dissolved in water can hardly be degraded in the environment, which have a serious and long-term toxic threat to amphibians and aquatic lives, eventually humans.[10] Pal's group firstly identified the model reduction of *p*-NP to *p*-AP by sodium borohydride ($NaBH_4$) for evaluating the catalytic activity of nanoparticles.[11] As an efficient reducing agent, $NaBH_4$ is safer, more useful and convenient in dealing with water-soluble aromatic pollutants compared with other reducing agents, e.g. hydrogen.[12, 13]

In recent years, noble metal nanoparticles especially bimetals have attracted great interest because of their potential applications in many fields such as electrochemistry,[14] electronics,[15] magnetic storage,[16] sensing,[17] optics,[18] and

catalysis.[19] Among them, Pt-based nanostructures, particularly alloying with transition metals, have received widespread research attention thanks to their high catalytic activity for many industrially important reactions.[20] For example, PtNi,[21] PtFe,[22] PtCu,[23] and PtCo[24] were prepared and used as high-performance hybrid electrocatalysts in the literature. Goodman's group found that Ni-Pt surfaces with Ni coverage in the monolayer regime showed higher hydrogenolysis activity than those of their individual counterparts (i.e., single Ni and Pt).[25] The improved catalytic activity is attributed to the synergetic effects such as geometric and electronic effects originated from the lattice contraction and downshift of the d-band center of Pt in the bimetallic structures.[14]

Graphene oxide (GO) has many oxygen-containing functional groups on its surface such as hydroxyl, epoxide, carbonyl, and carboxyl groups, which provide chemically active sites available for metal nanoparticles anchoring and dispersion.[26, 27] It is also beneficial to avoid metal nanoparticles from aggregation, thereby resulting into highly dispersed metal nanoparticles with ultra-small sizes. Moreover, GO is a low-cost carbon material that can be easily reduced to graphene. In addition, graphene-supported Pt-based catalysts demonstrate improved catalytic performances and undergo less poisoning by CO-like intermediates during methanol oxidation reaction as compared to those supported on commercial carbon black.[28]

Herein, a simple and facile hydrothermal method was developed for one-pot synthesis of PtNi nanosnowflakes anchored on reduced graphene oxide (RGO). The catalytic performance of PtNi nanosnowflakes/RGO was also investigated, using the

hydrogenation of *p*-NP as a model system.

2. Experimental section

2.1 Chemicals

Graphite powder (8000 mesh, for which the diameter is about 1-2 μm), nickel chloride hexahydrate ($NiCl_2 \cdot 6H_2O$), chloroplatinic acid (H_2PtCl_6), polyvinyl pyrrolidone (PVP), N, N-dimethylformamide (DMF), ethylenediamine (EDA), commercial Pt/C (10 wt. %), and *p*-nitrophenol (*p*-NP) were purchased from Aladdin Chemistry Co. Ltd (Shanghai, China). All the other chemicals were of analytical grade and used without further purification. All the aqueous solutions were prepared with twice-distilled water in the whole experiments.

2.2 Synthesis of PtNi nanosnowflakes/RGO

Graphene oxide (GO) was firstly prepared from natural graphite powder *via* the acid-oxidation process, according to the modified Hummers' method.[29] The resultant was further sonicated for 30 min to obtain the exfoliated GO for use.

For typical preparation of PtNi nanosnowflakes/RGO, 5 mL of GO suspension (1 mg mL^{-1}) and 200 mg of PVP were firstly put into 15 mL of DMF, and the mixture was constantly stirred for 10 min. Then, 9.2 mg of $NiCl_2$ and 1 mL of H_2PtCl_6 (38.62 mM) were dissolved into the mixture under gentle agitation, followed by the slow drop-wise addition of 0.2 mL of EDA under stirring. The mixture was transferred into a 25 mL Teflon-lined autoclave, maintained at 160 °C for 10 h, and then cooled to

room temperature naturally. The resulting black precipitates were collected by centrifugation and thoroughly washed with ethanol for several times, and dried at 60 °C in vacuum for further characterization.

2.3 Characterization

The morphology and microstructure of the samples were determined by transmission electron microscopy (TEM) and high-resolution TEM (HR-TEM) on a JEM-2100F transmission electron microscope operating at an acceleration voltage of 200 kV attached with selective area electron diffraction (SAED) and energy dispersive X-ray spectrometer (EDS). The elemental mappings were recorded on the scanning transmission electron microscope (STEM) with a high-angle annular dark-field (HAADF) detector (HITACHI S-5500). X-ray diffraction (XRD) measurements were performed on a Rigaku Dmax-2000 diffractometer using Cu Kα radiation source (λ = 0.15418 nm). X-ray photoelectron spectroscopy (XPS) measurements were performed to study the surface properties on a K-Alpha XPS (ThermoFisher, E. Grinstead, UK) with an Al Kα X-ray radiation (1486.6 eV photons) for excitation. Raman experiments were performed with a Renishaw Raman system model 1000 spectrometer equipped with a CCD detector, equipped with a He/Ne laser at a wavelength of 633 nm. Thermogravimetric analysis (TGA) was performed in air on a NETZSCH STA 449C thermogravimetric analyzer. The samples were heated from the temperature of 25 to 900 °C with the heating rate of 10 °C min^{-1}.

2.4 General procedure for *p*-nitrophenol reduction

Typically, 300 μL of *p*-nitrophenol solution (0.7 mM) was placed into 1 mL of freshly-prepared $NaBH_4$ solution (0.5 M) with 1 mL of water in a quartz cuvette. The mixed solution turned yellow. After the injection of PtNi nanosnowflakes/RGO suspension (1 mg mL^{-1}) into the cuvette, the mixed solution was immediately measured by UV-vis spectroscopy in a scanning range of 250-550 nm. There is an absorption peak emerged at 400 nm, and its spectral changes were monitored by UV-vis spectra as a function of time. The color of the reaction solution changed from yellow to colorless by prolonging the reaction time. Following the similar procedures, commercial Pt/C (10 wt. %, 1 mg mL^{-1}) was also used as a heterogeneous catalyst for *p*-nitrophenol reduction in control experiments, while the other experimental conditions were kept constant.

3. Results and discussion

Fig. 1 shows the morphologies of the typical samples characterized by transmission electron microscopy (TEM). Evidently, there are many well-defined snowflake-like PtNi nanocrystals uniformly dispersed on reduced graphene oxide nanosheets (Fig. 1A-B). The snowflake-like PtNi nanostructures possess many elongated crystalline grains, which extend from the surface to enlarge the surface area. High-resolution TEM (HRTEM) image (Fig. 1C) reveals well-defined fringes of PtNi nanosnowflakes taken from the marked regions with the interplanar distances of 0.214 nm and 0.194 nm, corresponding to the (111) and (200) crystal planes of PtNi nanosnowflakes, respectively. These values are smaller than those of the face-centered

cubic (*fcc*) Pt (0.227 nm and 0.196 nm, JCPDS-04-0802), but larger than those of the *fcc* Ni (0.203 nm and 0.176 nm, JCPDS-46-0850), reflecting the formation of PtNi alloy.[30] This is ascribed to the contraction of the lattice via the substitution of Pt with Ni atoms.[31]

HAADF-STEM-EDS measurements were conducted to determine the elemental distribution in PtNi nanosnowflakes. According to the elemental mapping images (Fig. 2A-C) and cross-sectional compositional line profiles of a PtNi snowflake (Fig. 2D), Pt and Ni elements are homogeneously distributed throughout the entire particle. Furthermore, EDS analysis demonstrates the coexistence of Pt and Ni elements in PtNi nanosnowflakes (Fig. S1, Electronic Supplementary Information, ESI). These results strongly manifest the formation of PtNi alloy,[32] which is in good agreement with HRTEM analysis. In addition, the atomic ratio of Pt to Ni is estimated to be 2:3 (inset in Fig. S1). The larger amount of Ni than Pt in PtNi nanosnowflakes may facilitate the relaying of electrons to the substrate and enhance the catalytic activity accordingly.[33]

The well-alloyed PtNi nanosnowflakes were further confirmed by XRD experiments (Fig. 3). There are four strong diffraction peaks detected at 40.06°, 46.84°, 68.41°, and 82.48°, which are well attributed to the (111), (200), (220), and (311) crystal planes of PtNi nanosnowflakes, respectively (Fig. 3, curve a). This is no evidence found of pure Pt, Ni, or any oxide phases in the XRD spectrum of PtNi nanosnowflakes. It should be noted that the diffraction peaks slightly shift to higher diffraction angles for PtNi nanosnowflakes in contrast with pure Pt, which reveals that

Ni has entered into Pt lattice and the formation of PtNi alloy.[21, 34]

Besides, a broad peak shows up at around 24.13°, which is indexed to the (002) crystal planes of graphene,[31] which is unlike blank GO with a sharp peak centered at 11.0° (Fig. 3, curve b), indicating the efficient reduction of GO to RGO. As a consequence, the formation of RGO is beneficial to improve the electrical conductivity of PtNi nanosnowflakes/RGO.

Fig. 4A shows Raman spectra of PtNi nanosnowflakes/RGO (curve a) and GO (curve b). There are two main characteristic peaks observed at 1335 and 1594 cm^{-1} for both cases, which are correlated with the *D* band because of disorder features induced by lattice defect and the *G* band associated with the first-order scattering of the E_{2g} vibrational mode within aromatic carbon rings.[35] And the intensity ratio of *D* to *G* bands (I_D/I_G) is inversely proportional to the degree of disorder and the average size of the in-plane sp^2 domains.[36] The I_D/I_G is estimated to be 1.13 for PtNi nanosnowflakes/RGO, which is larger than that of GO (0.92) under the identical conditions, reflecting that the in-plane sp^2 domains become smaller when the GO is effectively reduced to RGO.[37] This result again demonstrates the effective reduction of GO.

The thermal stability of PtNi nanosnowflakes/RGO was investigated by TGA and differential scanning calorimetry (DSC) measurements (Fig. 4B). The weight loss between 200 and 400 °C for GO (curve b) is attributed to the removal of some oxygen-containing functional groups.[38] However, there is a small weight loss observed for PtNi nanosnowflakes/RGO (curve a) under the identical conditions,

different from that of GO. Meanwhile, no exothermic peak was observed in DSC curve of PtNi nanosnowflakes/RGO from 200 to 400 ℃ (curve a'). It indicates a gradual decrease in the amount of oxygen-containing functional groups and a profound reduction of GO to RGO in PtNi nanosnowflakes/RGO. Moreover, the steep slope from 420 °C to 600°C is ascribed to the complete combustion of GO to CO or CO_2.[39] The metal loading is 13.63 % for PtNi nanosnowflakes/RGO. Furthermore, EDS analysis demonstrates that the weight ratio of Pt to Ni is about 7:3. Then, the content of Pt and Ni in PtNi nanosnowflakes/RGO is about 9.37 % and 4.26 %, respectively.

XPS analysis was employed to investigate the chemical properties of PtNi nanosnowflakes/RGO (Fig. 5). As illustrated by the high-resolution Pt 4f XPS spectrum (Fig. 5A), the diffraction peaks at the binding energy of 70.71 eV (Pt $4f_{7/2}$) and 73.94 eV (Pt $4f_{5/2}$) are assigned to metallic Pt and the ones at 72.66 eV (Pt $4f_{7/2}$) and 76.21 eV (Pt $4f_{5/2}$) correspond to Pd^{2+} species of PtO and $Pt(OH)_2$.[40, 41] By measuring the peaks intensities, it is found that Pt^0 is the predominant species in PtNi nanosnowflakes.[42] The corresponding peak positions negatively shift in contrast to those of pure Pt, indicating the modification of the electronic structures of Pt when it was alloyed with Ni.[43]

Fig. 5B displays the correlated Ni 2p XPS spectrum, which shows a complex structure with its characteristic intense shake-up satellite signal of high binding energy adjacent to the main peaks. After the shake-up satellite signal was considered, The peaks at 855.18 eV (Ni $2p_{3/2}$) and 872.93 eV (Ni $2p_{1/2}$) are ascribed to $Ni(OH)_2$,

and the ones at 856.33 eV (Ni $2p_{3/2}$) and 874.03 eV (Ni $2p_{1/2}$) are attributed to NiOOH.[44] By estimating the correlated peak intensities, it is obvious that Ni^0 on the surface of the nanoflakes was low irrespective, which is related to method of preparation. These observations appear to be a characteristic of Pt based bimetallic nanomaterials in the previous report.[21, 45]

Similarly, the peak of C 1s was further separated into three peaks at 284.7, 285.8, and 287.7 eV (Fig. 5C), corresponding to the C–C (sp^2), C–O, and C=O groups, respectively.[36, 46, 47] Clearly, the bands associated with oxygen functional groups are much weaker and the peak from C–C bond is much stronger for PtNi nanosnowflakes/RGO as compared to those of single GO (Fig. S2, ESI), indicating that GO is well deoxygenated, which is in good accordance with Raman measurements.

It is known that *p*-aminophenol (*p*-AP) is a commercially important intermediate for the fabrication of analgesic and antipyretic drugs, anticorrosion lubricants, and hair drying agents.[1] Furthermore, *p*-nitrophenol (*p*-NP) shows a distinct UV-vis absorbance peak at 317 nm in water, which can be employed as an instructive peak to examine the catalytic activity of PtNi nanosnowflakes/RGO.

Typically, the UV-vis absorbance peak shift to 400 nm immediately after the addition of $NaBH_4$, owing to the formation of *p*-nitrophenolate ions (Fig. S3, ESI).[48] Then, the total reduction reaction is summarized in the follow equation:

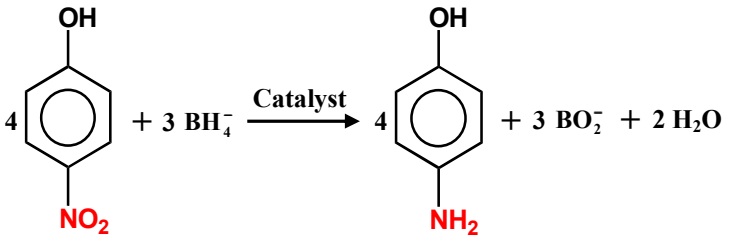

(1)

Although the reaction is thermodynamically feasible considering the E_0 for *p*-NP/*p*-AP (–0.76 V *vs.* NHE) and H_3BO_3/BH_4^- (–1.33 V *vs.* NHE), it is kinetically restricted in the absence of a catalyst.[49] However, the absorbance peak intensity at 400 nm decreases rapidly in the presence of PtNi nanosnowflakes/RGO, and a new peak appears at 300 nm because of the formation of *p*-AP (Fig. 6). And the new peak intensity is increased by extending the reaction time. The intensity of the absorbance peak at 400 nm decreased to nearly zero, suggesting the completion of the reaction.

Specifically, *p*-NP can be efficiently reduced within 10 min by using 0.05 mg PtNi nanosnowflakes/RGO (Fig. 6A). As expected, the catalytic time is extended by reducing the dosage of PtNi nanosnowflakes/RGO (Fig. 6B-C). Fig. 7 displays the time-dependent UV-vis absorption spectra for the reduction of *p*-NP in the presence of PtNi nanosnowflakes/RGO, using commercial Pt/C as a standard material. The peak emerged at 400 nm disappears completely within 10 min for PtNi nanosnowflakes/RGO (Fig. 7A). The reaction time is much shorter than that of commercial Pt/C under the identical conditions (50 min, Fig. 7B).

In this study, sufficient $NaBH_4$ is existed in the reaction system, it is reasonable to assume that the change of $NaBH_4$ concentration is negligible during the reaction

system.[50] Besides, the abundant of $NaBH_4$ might benefit to protect *p*-AP from aerial oxidation.[51] As a result, a pseudo-first-order kinetics equation was applied to calculate the apparent rate constant (k_a):

$$\ln(A_t/A_0) = \ln(C_t/C_0) = k_a\, t \quad (2)$$

where C_0 is the concentration of *p*-NP at initial time and C_t is the concentration of *p*-NP at time *t*, and k_a is the catalytic reduction apparent rate constant, while C_0 and C_t would be calculated from the absorbance intensity of *p*-NP at time initiation (A_0) and *t* (A_t). Fig. 7C provides the plots of $\ln(A_t/A_0)$ *vs*. reaction time of PtNi nanosnowflakes/RGO and commercial Pt/C, which fit well with the pseudo-first-order kinetics model as expected. Calculating from the slopes of the plots, the k_a values of PtNi nanosnowflakes/RGO and commercial Pt/C are 2.17×10^{-3} s^{-1} and 1.3×10^{-3} s^{-1}, respectively.

However, in order to compare the catalytic activity with different catalysts in the previous reports, k_a should be further normalized to another comparable kinetic parameters, k_n, which can be defined as,[50]

$$k_n = (10^{-3}\, c_0 V/m)\; k_a \quad (3)$$

where c_0 (mM) is the initial concentration of *p*-NP, and *V* (mL) is the volume of the reactant solution, and *m* (g) is the metal mass of the catalysts. According to the traditional theory about the catalytic reduction of *p*-NP to *p*-AP, electron transfer occurs from BH_4^- to *p*-NP via the adsorption of the reactant molecules onto the catalyst surface (e.g. PtNi nanosnowflakes). Fig. 8 exhibits the postulate mechanism of the catalytic reduction of *p*-NP with PtNi nanosnowflowers/RGO. It is found that

the dosage of *p*-NP influences the values of k_a or k_a/m in the present study. Thus, the coefficient $10^{-3}\ c_0V$ was introduced to make a rational performance evaluation per gram of catalyst. As a result, the k_n value of PtNi nanosnowflakes was calculated to be 67×10^{-3} mmol s^{-1} g^{-1}, which is larger than commercial Pt/C (54×10^{-3} mmol s^{-1} g^{-1}). Furthermore, this value is higher than those of Ag nanoparticles (23×10^{-3} mmol s^{-1} g^{-1}),[52] dentritic $NiCo_2$ alloy (1.2×10^{-3} mmol s^{-1} g^{-1}),[3] and $Pt_{20}Ni_{80}$ (45×10^{-3} mmol s^{-1} g^{-1}).[33]

Catalyst reusability is an important issue in practical catalytic applications. The stability of PtNi nanosnowflakes/RGO has been investigated by recycling test under the same condition (Fig. 9 and S4, ESI). After each measurement, the catalyst was recovered by centrifugation and followed by washing with twice-distilled water for the next cycle of catalysis. As shown in Fig. 9, more than 86.2 % of *p*-NP molecules are converted to *p*-AP over the same time period after five cycles. It means that there is no obvious loss of catalytic activity for the catalyst after the recycling test. Besides, as illustrated by TEM measurements, the morphology of PtNi nanosnowflakes/RGO is almost retained and nearly no agglomeration observed after the recycling measurements (Fig. S5, ESI), showing better stability and superior catalytic activity of PtNi nanosnowflakes/RGO for *p*-NP reduction.

The improved performances of PtNi nanosnowflakes/RGO are attributed to the following reasons: (1) the charge density of d-band was modified with the electronic influence of Ni in PtNi nanosnowflakes, which can facilitate the relaying of electrons to the substrate from borohydride ions and enhance the catalytic activity;[14, 33] (2) the

unique structures of PtNi nanosnowflakes endow more activity sites available for the adsorption of reactant molecules; (3) the enlarged surface area and high conductivity of RGO benefit the reactant adsorption and electron transfer.[26]

4. Conclusions

In summary, well-dispersed PtNi nanosnowflakes/RGO was prepared by a simple hydrothermal method, with the help of DMF as the solvent and reductant, and ethylenediamine as the surfactant and capping agent. The resulting nanocomposites exhibited remarkably enhanced catalytic activity and better stability in comparison with those of commercial Pt/C (10 wt %) in the catalytic reduction of *p*-NP. It is demonstrated that the developed method is efficient and green for the conversion of *p*-NP to *p*-AP in aqueous media under mild conditions, which might shed light for the fabrication of other nanocatalysts and broaden their applications in the future.

Acknowledgement

This work was financially supported by National Natural Science Foundation of China (Nos. 21475118, 21175118, 21275130 and 21275131).

References

1. Y. Du, H. Chen, R. Chen and N. Xu, *Appl. Catal., A*, 2004, **277**, 259-264.
2. S. Saha, A. Pal, S. Kundu, S. Basu and T. Pal, *Langmuir*, 2009, **26**, 2885-2893.
3. K.-L. Wu, X.-W. Wei, X.-M. Zhou, D.-H. Wu, X.-W. Liu, Y. Ye and Q. Wang, *J.*

Phys. Chem. C, 2011, **115**, 16268-16274.

4. T. R. Mandlimath and B. Gopal, *J. Mol. Catal. A: Chem.*, 2011, **350**, 9-15.
5. C. V. Rode, M. J. Vaidya and R. V. Chaudhari, *Org. Process Res. Dev.*, 1999, **3**, 465-470.
6. H. Lu, H. Yin, Y. Liu, T. Jiang and L. Yu, *Catal. Commun.*, 2008, **10**, 313-316.
7. M. J. Vaidya, S. M. Kulkarni and R. V. Chaudhari, *Org. Process Res. Dev.*, 2003, **7**, 202-208.
8. T. Sun, Z. Zhang, J. Xiao, C. Chen, F. Xiao, S. Wang and Y. Liu, *Sci. Rep.*, 2013, **3**, 2527.
9. Z. Zhang, F. Xiao, J. Xi, T. Sun, S. Xiao, H. Wang, S. Wang and Y. Liu, *Sci. Rep.*, 2014, **4**, 4053.
10. P. Herves, M. Perez-Lorenzo, L. M. Liz-Marzan, J. Dzubiella, Y. Lu and M. Ballauff, *Chem. Soc. Rev.*, 2012, **41**, 5577-5587.
11. N. Pradhan, A. Pal and T. Pal, *Colloids Surf., A*, 2002, **196**, 247-257.
12. H. I. Schlesinger, H. C. Brown, A. E. Finholt, J. R. Gilbreath, H. R. Hoekstra and E. K. Hyde, *J. Am. Chem. Soc.*, 1953, **75**, 215-219.
13. H. Hu, J. H. Xin, H. Hu, X. Wang, D. Miao and Y. Liu, *J. Mater. Chem. A*, 2015.
14. V. R. Stamenkovic, B. S. Mun, M. Arenz, K. J. J. Mayrhofer, C. A. Lucas, G. Wang, P. N. Ross and N. M. Markovic, *Nat. Mater.*, 2007, **6**, 241-247.
15. Y. Jo, I. Jung, N. Kim and H. Lee, *J. Nanopart. Res.*, 2012, **14**, 1-10.
16. N. A. M. Barakat, K. A. Khalil, I. H. Mahmoud, M. A. Kanjwal, F. A. Sheikh and H. Y. Kim, *J. Phys. Chem. C*, 2010, **114**, 15589-15593.

17. F. Xiao, F. Zhao, D. Mei, Z. Mo and B. Zeng, *Biosens. Bioelectron.*, 2009, **24**, 3481-3486.

18. D. Phanon, B. Bentria, D. Benbertal, A. Mosset and I. Gautier-Luneau, *Solid State Sci.*, 2006, **8**, 1466-1472.

19. C. Della Pina, E. Falletta and M. Rossi, *J. Catal.*, 2008, **260**, 384-386.

20. W. Yu, M. D. Porosoff and J. G. Chen, *Chem. Rev.*, 2012, **112**, 5780-5817.

21. T. C. Deivaraj, W. Chen and J. Y. Lee, *J. Mater. Chem.*, 2003, **13**, 2555-2560.

22. A. K. Shukla, R. K. Raman, N. A. Choudhury, K. R. Priolkar, P. R. Sarode, S. Emura and R. Kumashiro, *J. Electroanal. Chem.*, 2004, **563**, 181-190.

23. P. Mani, R. Srivastava and P. Strasser, *J. Phys. Chem. C*, 2008, **112**, 2770-2778.

24. L. Liu, E. Pippel, R. Scholz and U. Gösele, *Nano Lett.*, 2009, **9**, 4352-4358.

25. D. W. Goodman, *Ultramicroscopy*, 1990, **34**, 1-9.

26. X. Huang, X. Qi, F. Boey and H. Zhang, *Chem. Soc. Rev.*, 2012, **41**, 666-686.

27. S.-S. Li, J. Yu, Y.-Y. Hu, A.-J. Wang, J.-R. Chen and J.-J. Feng, *J. Power Sources*, 2014, **254**, 119-125.

28. L. Dong, R. R. S. Gari, Z. Li, M. M. Craig and S. Hou, *Carbon*, 2010, **48**, 781-787.

29. M. Choucair, P. Thordarson and J. A. Stride, *Nat. Nano*, 2009, **4**, 30-33.

30. L. Li, Y. Wu, J. Lu, C. Nan and Y. Li, *Chem. Commun.*, 2013, **49**, 7486-7488.

31. Y. Hu, P. Wu, Y. Yin, H. Zhang and C. Cai, *Appl. Catal., B*, 2012, **111–112**, 208-217.

32. W. Wang, D. Wang, X. Liu, Q. Peng and Y. Li, *Chem. Commun.*, 2013, **49**,

2903-2905.

33. S. K. Ghosh, M. Mandal, S. Kundu, S. Nath and T. Pal, *Appl. Catal., A*, 2004, **268**, 61-66.

34. Z.-C. Wang, Z.-M. Ma and H.-L. Li, *Appl. Surf. Sci.*, 2008, **254**, 6521-6526.

35. X.-Y. Yan, X.-L. Tong, Y.-F. Zhang, X.-D. Han, Y.-Y. Wang, G.-Q. Jin, Y. Qin and X.-Y. Guo, *Chem. Commun.*, 2012, **48**, 1892-1894.

36. J.-N. Zheng, J.-J. Lv, S.-S. Li, M.-W. Xue, A.-J. Wang and J.-J. Feng, *J. Mater. Chem. A*, 2014, **2**, 3445-3451.

37. M. A. Pimenta, G. Dresselhaus, M. S. Dresselhaus, L. G. Cancado, A. Jorio and R. Saito, *Phys. Chem. Chem. Phys.*, 2007, **9**, 1276-1290.

38. J.-X. Feng, Q.-L. Zhang, A.-J. Wang, J. Wei, J.-R. Chen and J.-J. Feng, *Electrochim. Acta*, 2014, **142**, 343-350.

39. S. Sharma, A. Ganguly, P. Papakonstantinou, X. Miao, M. Li, J. L. Hutchison, M. Delichatsios and S. Ukleja, *J. Phys. Chem. C*, 2010, **114**, 19459-19466.

40. J. Yang, W. Zhou, C. H. Cheng, J. Y. Lee and Z. Liu, *ACS Appl. Mat. Interfaces*, 2009, **2**, 119-126.

41. J.-J. Lv, J.-X. Feng, S.-S. Li, Y.-Y. Wang, A.-J. Wang, Q.-L. Zhang, J.-R. Chen and J.-J. Feng, *Electrochim. Acta*, 2014, **133**, 407-413.

42. J.-N. Zheng, S.-S. Li, X. Ma, F.-Y. Chen, A.-J. Wang, J.-R. Chen and J.-J. Feng, *J. Mater. Chem. A*, 2014, **2**, 8386-8395.

43. G.-J. Wang, Y.-Z. Gao, Z.-B. Wang, C.-Y. Du, J.-J. Wang and G.-P. Yin, *J. Power Sources*, 2010, **195**, 185-189.

44. A. P. Grosvenor, M. C. Biesinger, R. S. C. Smart and N. S. McIntyre, *Surf. Sci.*, 2006, **600**, 1771-1779.

45. K.-W. Park, J.-H. Choi, B.-K. Kwon, S.-A. Lee, Y.-E. Sung, H.-Y. Ha, S.-A. Hong, H. Kim and A. Wieckowski, *J. Phys. Chem. B*, 2002, **106**, 1869-1877.

46. C. C. Li, H. Yu, Q. Yan and H. H. Hng, *J. Power Sources*, 2015, **274**, 310-317.

47. Z. Zhang, T. Sun, C. Chen, F. Xiao, Z. Gong and S. Wang, *ACS Appl. Mat. Interfaces*, 2014, **6**, 21035-21040.

48. H. Li, L. Han, J. Cooper-White and I. Kim, *Green Chem.*, 2012, **14**, 586-591.

49. Z. Jiang, D. Jiang, A. M. Showkot Hossain, K. Qian and J. Xie, *Phys. Chem. Chem. Phys.*, 2015, **17**, 2550-2559.

50. J. Liu, Q. Wu, F. Huang, H. Zhang, S. Xu, W. Huang and Z. Li, *RSC Adv.*, 2013, **3**, 14312-14321.

51. K. Hayakawa, T. Yoshimura and K. Esumi, *Langmuir*, 2003, **19**, 5517-5521.

52. P. Zhang, C. Shao, Z. Zhang, M. Zhang, J. Mu, Z. Guo and Y. Liu, *Nanoscale*, 2011, **3**, 3357-3363.

Captions

Fig. 1. (A-B) TEM and (C) HRTEM images of PtNi nanosnowflowers/RGO. Inset in A shows the corresponding SAED pattern.

Fig. 2. (A-C) HAADF-STEM-EDS elemental mapping images and (D) cross-sectional compositional line profiles taken from a single PtNi nanosnowflower.

Fig. 3. XRD patterns of PtNi nanosnowflowers/RGO and pure Pt.

Fig. 4. (A) Raman spectra and (B) TGA curves of PtNi nanosnowflowers/RGO (curve a) and GO (curve b). The dotted curve a' in B represent the DSC curve of PtNi nanosnowflowers/RGO

Fig. 5. High-resolution (A) Pt 4f, (B) Ni 4f, and (C) C 2p XPS spectra of PtNi nanosnowflowers/RGO.

Fig. 6. Time-dependent UV-vis spectral changes in *p*-NP catalyzed by different dosage of PtNi nanosnowflowers/RGO: (A) 0.05 mg; (B) 0.03 mg; and (C) 0.01 mg.

Fig. 7. Time-dependent UV-vis spectral changes in *p*-NP catalyzed by 0.05 mg of (A) PtNi nanosnowflowers/RGO and (B) commercial Pt/C. (C) The corresponding plots

of $\ln(A_t/A_0)$ *vs*. reaction time toward *p*-NP reduction.

Fig. 8. Schematic illustration of the catalytic reduction of *p*-NP with PtNi nanosnowflowers/RGO.

Fig. 9. The stability of PtNi nanosnowflowers/RGO for the catalytic reduction of *p*-NP during 5 cycles.

Figures

Fig. 1

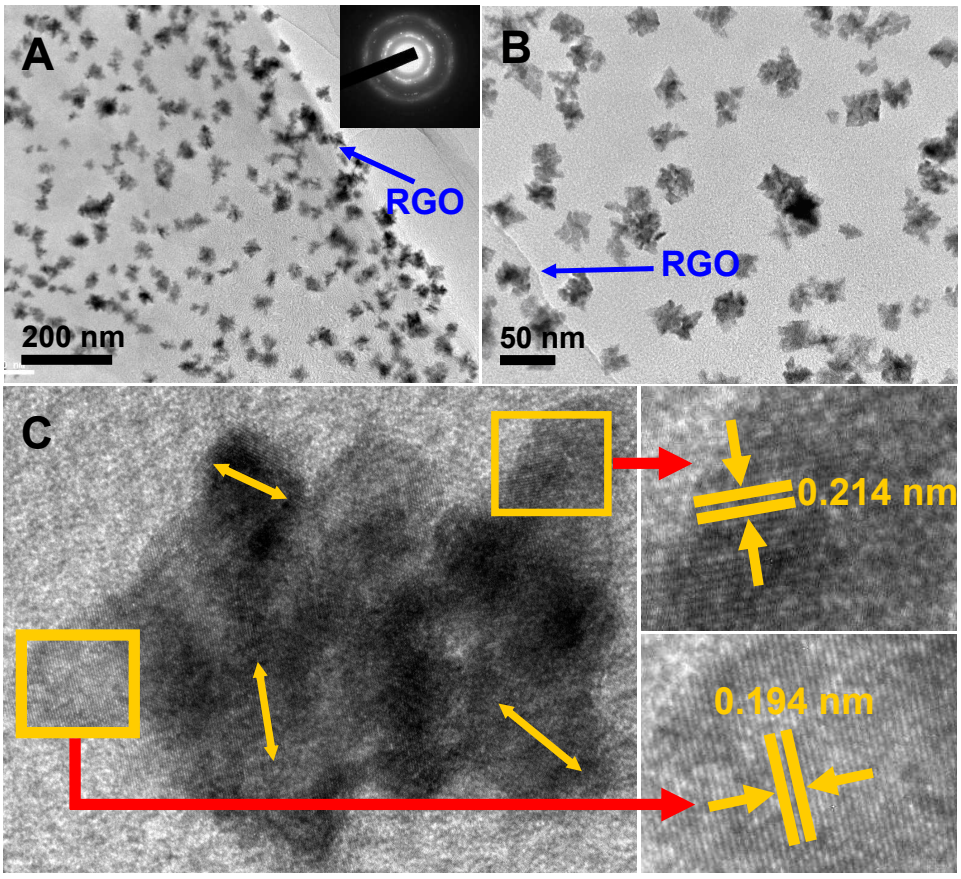

Fig. 2

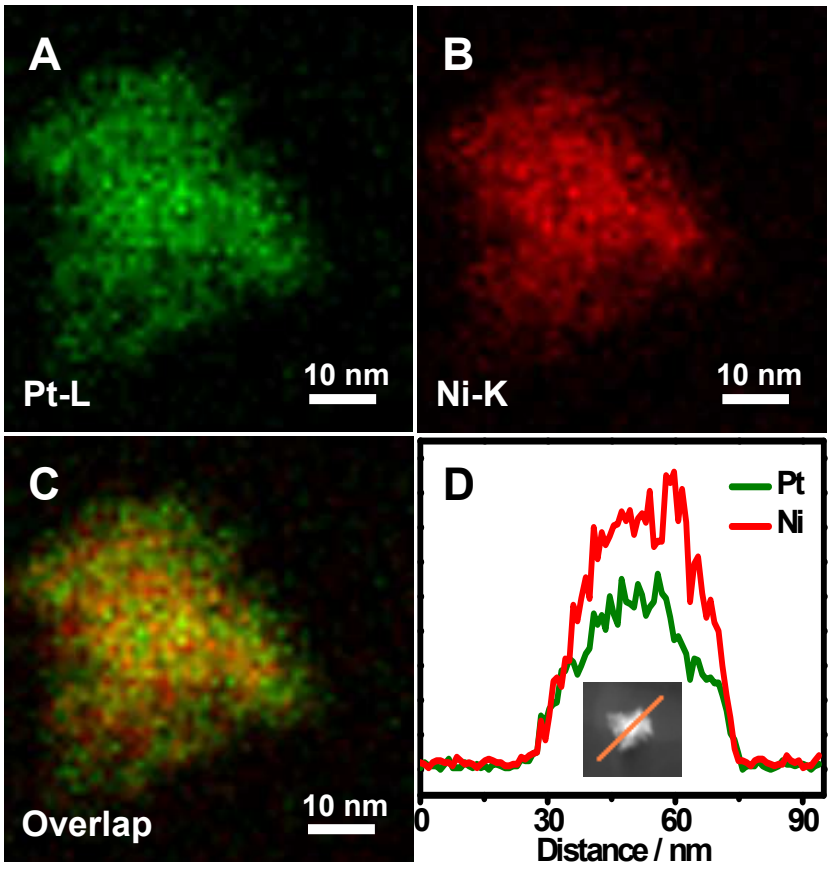

Fig. 3

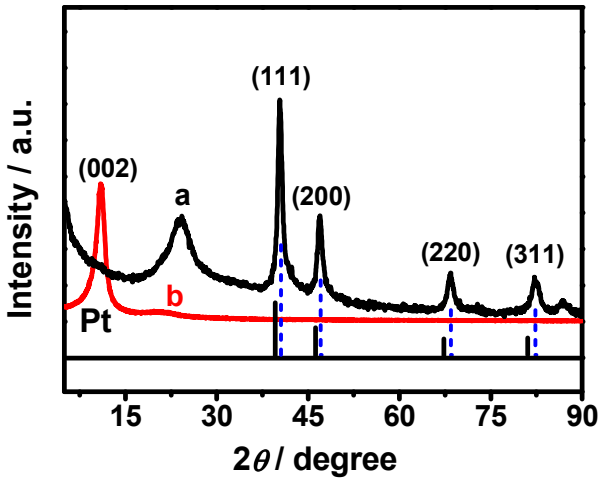

Fig. 4

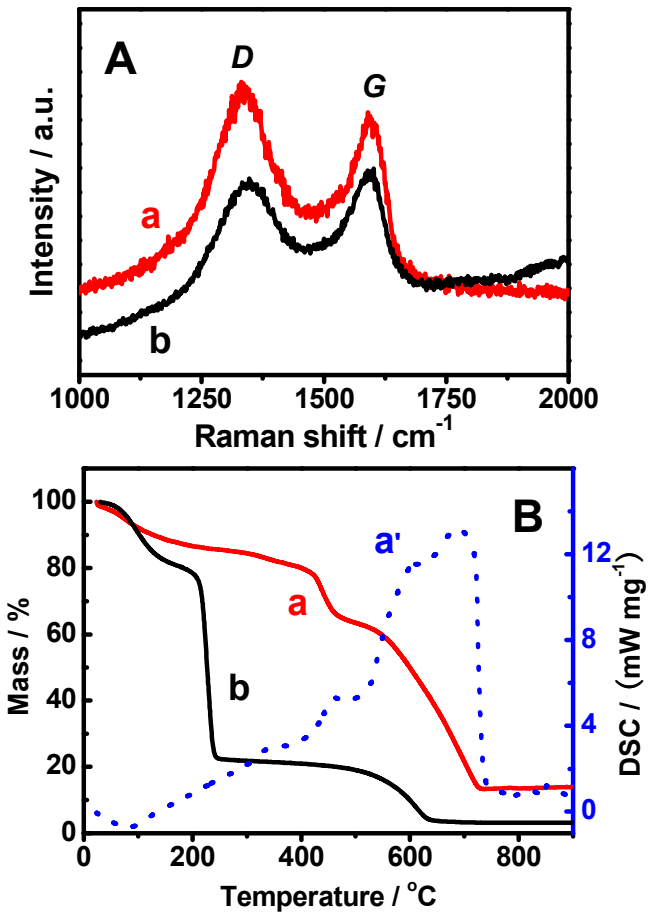

Fig. 5

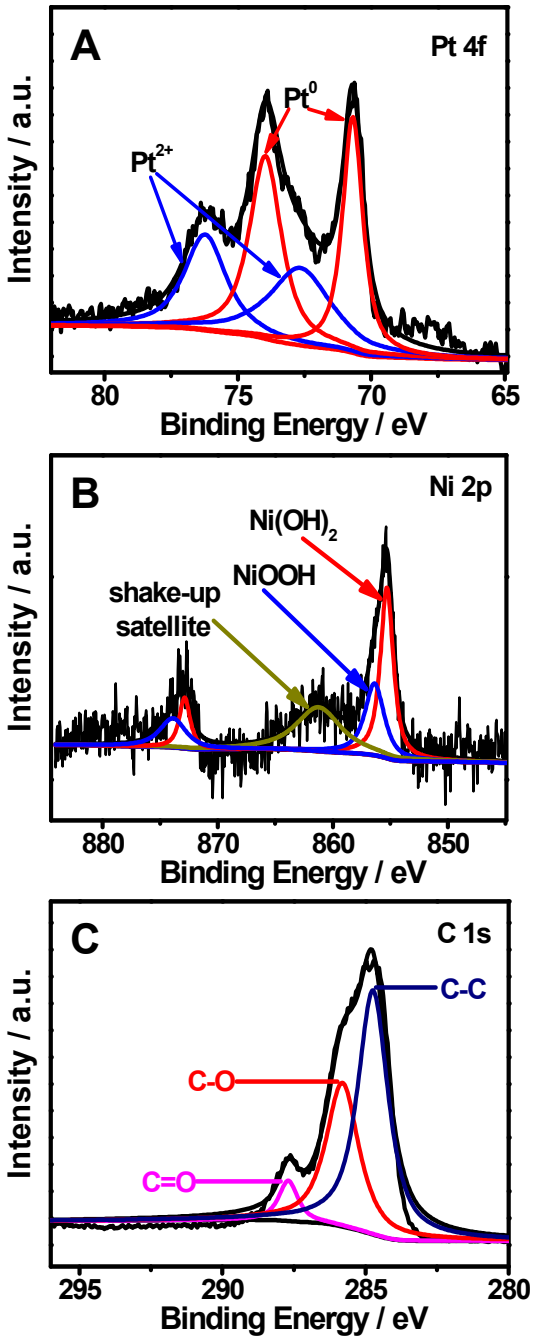

Fig. 6

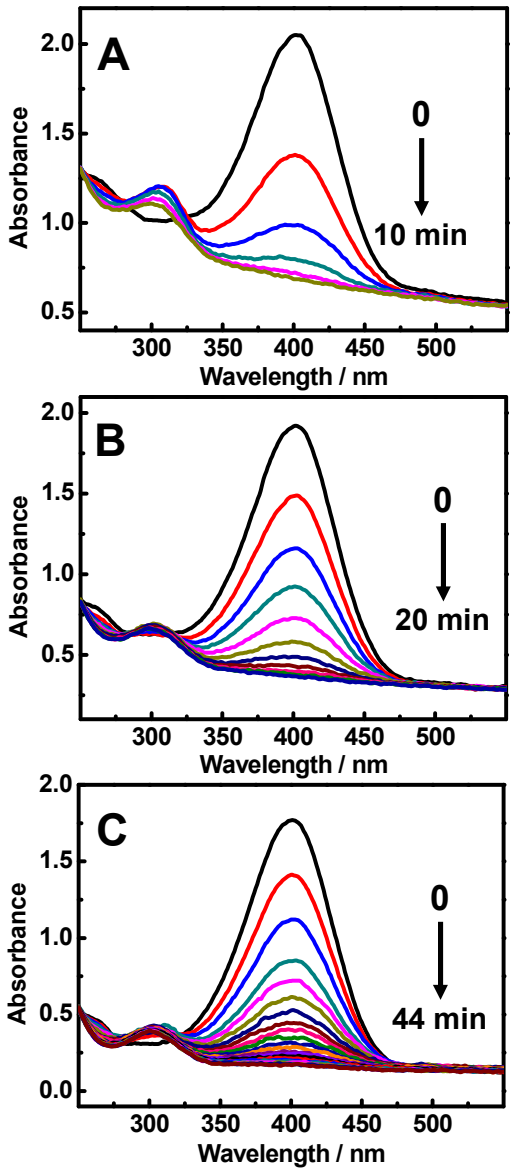

Fig. 7

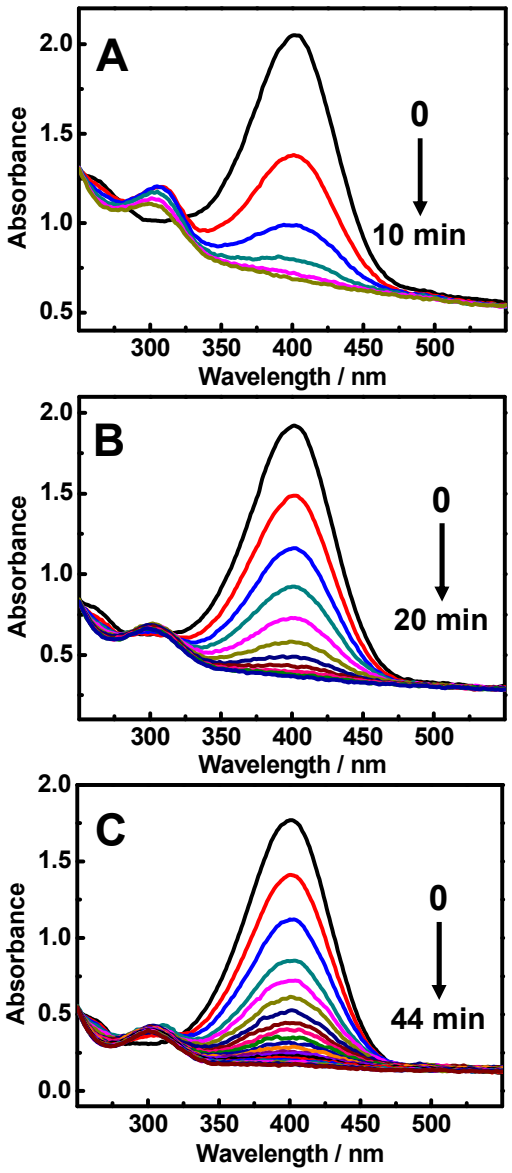

Fig. 8

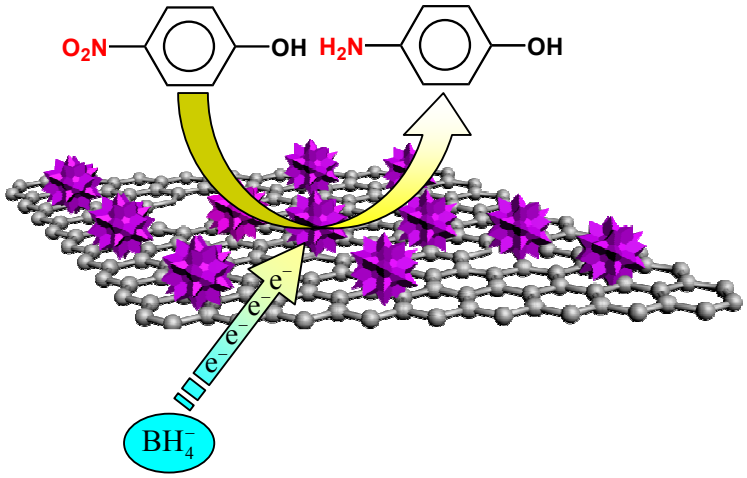

Fig. 9

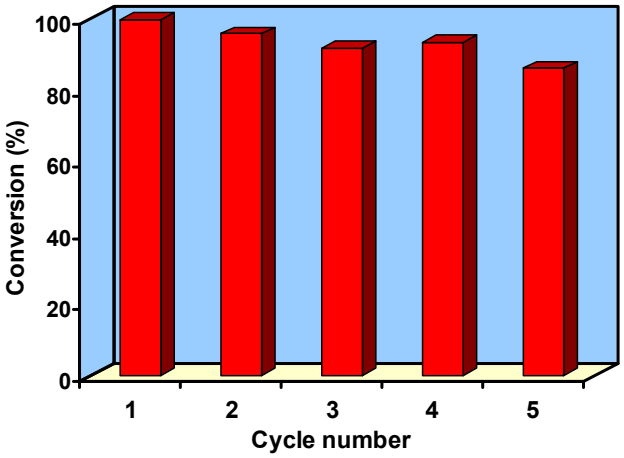

Graphical Abstract

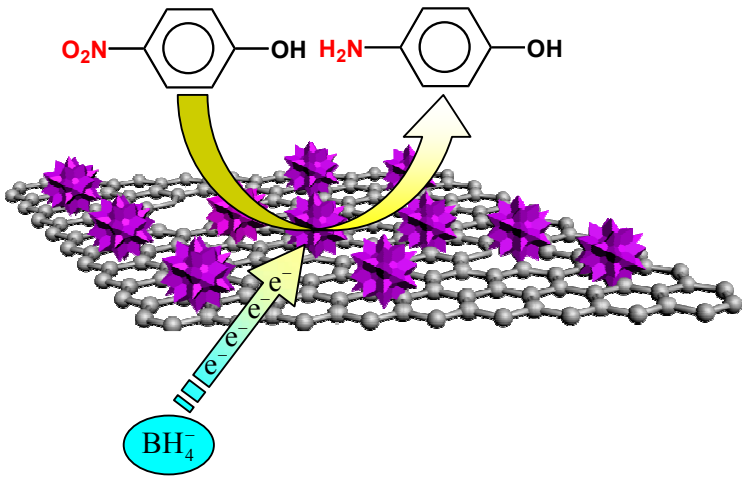

A facile hydrothermal strategy was developed for synthesis of PtNi alloyed nanosnowflakes supported on RGO using DMF as the solvent and reductant, and ethylenediamine as the structure-directing agent. The nanocomposites showed highly catalytic activity for *p*-nitrophenol reduction.